



Broadband hyperbolic plasmons in aluminum disulfide monolayer and its analogues: The role of orbital anisotropy

Shuting Hou , Mingzheng Wang, Han Gao, Chao Ding, Xuejin Zhang, Lei Sun, Xikui Ma, Yangyang Li, and Mingwen Zhao *

School of Physics, Shandong University, Jinan 250100, China



(Received 17 December 2022; accepted 24 April 2023; published 8 May 2023)

Two-dimensional (2D) materials with high in-plane anisotropy offer promising candidates for hosting highly directional surface plasmons, but few of them have been demonstrated to reach this goal thus far. In this paper, we propose a design principle of 2D hyperbolic materials (2D-HMs) based on orbital anisotropy and predict from first-principles calculations a family of 2D-HMs: aluminum disulfide monolayer and its analogues XY_2 ($X = \text{Al, Ga, In}$; $Y = \text{S, Se, Te}$). These natural 2D-HMs exhibit broadband hyperbolic regimes across the near-infrared to ultraviolet spectrum, enabling the propagation of highly directional hyperbolic surface plasmons. Undamped plasmons emerge along the x direction with the maximum wave vector of $\sim 0.16 \text{ \AA}^{-1}$ and frequency of 4.6 eV, whereas the plasmons along the y direction have low frequency ($< 0.6 \text{ eV}$) and decay rapidly to electron-hole pairs for the AlS_2 monolayer. By solving Maxwell's equation, we simulate the directional propagation of the surface waves with hyperbolic dispersion relations. We correlate the fascinating plasmonic properties with the unique electronic structures of these highly anisotropic 2D materials, which offers a promising strategy for the design of 2D-HMs.

DOI: [10.1103/PhysRevB.107.195410](https://doi.org/10.1103/PhysRevB.107.195410)

I. INTRODUCTION

Materials with highly anisotropic electronic and optical properties offer a promising platform for studying unusual physical scenarios that introduce concepts for next-generation electronic and optoelectronic devices. Hyperbolic materials (HMs) with principal components of opposite signs in their permittivity tensor are of particular interest due to their unique electromagnetic response characteristics, such as optical nanoscale cavities [1,2], spontaneous emission enhancement [2,3], nanoscale imaging [4,5], and full-angle negative refraction [6,7]. These interesting properties are closely related to the peculiar dispersion relation between frequency ω and wave vector k which is determined by the permittivity of medium ε (assuming $\varepsilon_{xx} = \varepsilon_{yy}$):

$$\frac{k_x^2}{\varepsilon_{zz}} + \frac{k_z^2}{\varepsilon_{xx}} = \left(\frac{\omega}{c}\right)^2. \quad (1)$$

Hyperbolic media have $\varepsilon_{xx} \times \varepsilon_{zz} < 0$, corresponding to a hyperbolic isofrequency surface, in sharp contrast to the elliptic isofrequency surfaces of conventional anisotropic materials with $\varepsilon_{xx} > 0$ and $\varepsilon_{zz} > 0$. According to the signs of permittivity, they are classified into type-I ($\varepsilon_{xx} < 0$ and $\varepsilon_{zz} > 0$) and type-II ($\varepsilon_{xx} > 0$ and $\varepsilon_{zz} < 0$). Most experimentally realized HMs are artificially built from metallic and dielectric media aligned in different patterns. However, there are also many naturally occurring materials with intrinsic anisotropy in in-plane and/or out-of-plane directions, such as graphite [8], hexagonal boron nitride (hBN) [9], metal-organic frameworks

[10], and so on [11,12]. These natural materials (NMs) offer several advantages over metamaterials, such as simpler manufacturing processes, lower interfacial scattering losses, and larger maximum propagation wavelengths, which are quite crucial for many applications [13–16].

The anisotropic electronic and optical properties of two-dimensional (2D) materials present a promising avenue for the development of natural HMs. The inherent nature of 2D materials allows for the implementation of the hyperbolic regime in a single sheet without the need for complicated substrate patterning. Studies have predicted that 2D-HMs can support highly directional hyperbolic surface plasmons [6]. Like bulk HMs, 2D-HMs require highly anisotropic electron motion, resulting in an inductive response along one optical axis and a capacitive response along the other axis. Additionally, to achieve the desired functionality, the energy loss due to light absorption in the hyperbolic regime must be minimized. The strict requirements on the electronic properties of 2D-HMs have led to the rarity of natural materials that meet these criteria. To date, only a few natural 2D-HMs, such as MoTe_2 [17,18], black phosphorus [19], MoOCl_2 [20], and copper borides [21], have been proposed. Unfortunately, highly directional hyperbolic surface plasmons have not yet been demonstrated in these materials, partly due to the low quality factor (Q) and limited hyperbolic regimes. Therefore, discovering 2D materials that meet the above criteria of highly anisotropic electron motion, resulting in an inductive/capacitive response, and minimal light absorption in the hyperbolic regime represents a challenging task in material design.

In this paper, we propose a design principle for 2D-HMs based on a simple tight-binding (TB) model of a honeycomb

*zmw@sdu.edu.cn

lattice of p_x orbitals and demonstrate the anisotropic (inductive/capacitive) response that arises from orbital anisotropy. Using first-principles calculations in combination with linear-response theory, we further predict a family of 2D-HMs with broadband hyperbolic regimes and exceptional plasmonic properties. Our analysis focuses on the aluminum disulfide monolayer and its analogues XY_2 ($X = \text{Al, Ga, In; } Y = \text{S, Se, Te}$). These materials exhibit undamped plasmons along the x direction with energy up to 4.6 eV, while plasmons along the y direction have low energy (< 0.6 eV), which can be attributed to the anisotropic electronic band structure. We also verify the directional propagation of surface waves with hyperbolic dispersion relations in the hyperbolic regime by solving Maxwell's equations. The broadband hyperbolic regimes from near-infrared to ultraviolet spectrum, high quality factors, and ultralow light absorption in these materials make them highly promising for supporting highly directional hyperbolic surface plasmons. The correlation between the anisotropic electronic structures and the intriguing plasmonic properties of these materials uncovered in this paper provides a promising strategy for the design of 2D-HMs.

II. METHOD AND COMPUTATIONAL DETAILS

We perform first-principles calculations using VASP [22] and GPAW code [23,24], applying density functional theory (DFT) with the projector augmented-wave method [25] for ion-electron interaction. The exchange-correlation functional is treated self-consistently using a generalized gradient approximation in the form developed by Perdew, Burke, and Ernzerhof [26]. We use plane waves with an energy cut-off of 500 eV to expand the Kohn-Sham wave function and apply a vacuum space of 30-Å thickness along the z direction to exclude the interactions between neighboring images. The structural relaxation and electronic properties calculations are carried out on a $11 \times 11 \times 1$ k -point grid with an energy convergence criterion of 10^{-6} eV. We fully relax the atomic coordinates and the lattice vectors until the Hellmann-Feynman forces are < 0.01 eV/Å without any symmetry constraints. We confirm that the selected settings converge effectively to determine the optimized lattice parameters and the electronic properties of the 2D materials under investigation. To calculate the subsequent optical conductivity, we employ a Wannier interpolation technique to obtain the maximally localized Wannier functions of the bands near the Fermi level.

The conductivity $\sigma_{\alpha\beta}(\omega)$ describes the linear response of the electrical current in the α direction to the electric field applied in the β direction. We consider a minimal model of the conductivity tensor of 2D materials:

$$\sigma = \begin{pmatrix} \sigma_{xx} & 0 \\ 0 & \sigma_{yy} \end{pmatrix}, \quad (2)$$

where the intraband electron motion and interband electron transition are involved:

$$\sigma_{\alpha\alpha}(\omega) = \sigma_{\alpha\alpha}^{\text{intra}}(\omega) + \sigma_{\alpha\alpha}^{\text{inter}}(\omega). \quad (3)$$

The intraband contribution is evaluated using the Drude model (we set $\hbar = 1$ hereafter) [27]:

$$\sigma_{\alpha\alpha}^{\text{intra}}(\omega) = \frac{i}{(\omega + i\eta)S} \sum_{k,n} \left(\frac{\partial E_{n,k}}{\partial k_\alpha} \right)^2 \left(-\frac{\partial f}{\partial E_{n,k}} \right). \quad (4)$$

The interband contribution given by using the Kubo formalism reads [28]

$$\sigma_{\alpha\alpha}^{\text{inter}}(\omega) = \frac{i}{S} \sum_{\mathbf{k}, n \neq n'} \frac{f(E_{n,\mathbf{k}}) - f(E_{n',\mathbf{k}})}{(E_{n',\mathbf{k}} - E_{n,\mathbf{k}}) - (\omega + i\eta)} \frac{1}{E_{n',\mathbf{k}} - E_{n,\mathbf{k}}} \times |\langle \mathbf{k}, n | \hat{v}_\alpha | \mathbf{k}, n' \rangle|^2. \quad (5)$$

In these formulas, $|\mathbf{k}, n\rangle$ and $E_{n,\mathbf{k}}$ represent the wave function and energy of an electron at the n th band with the wave vector of \mathbf{k} , $f(E_{n,\mathbf{k}})$ is the Fermi distribution function, \hat{v}_α is the velocity operator, and S is the sample area.

The dielectric function and the collective excitation spectrum are computed using the linear response method. The noninteracting density response function in the reciprocal lattice space is specified by [29,30]

$$\chi_{GG'}^0(\mathbf{q}, \omega) = \frac{1}{\Omega} \sum_{\mathbf{k}, n, n'} \frac{f(E_{n,\mathbf{k}}) - f(E_{n',\mathbf{k}+\mathbf{q}})}{(E_{n,\mathbf{k}} - E_{n',\mathbf{k}+\mathbf{q}}) + \omega + i\eta} \times \langle \mathbf{k}, n | \exp[-i(\mathbf{q} + \mathbf{G}) \cdot \mathbf{r}] | \mathbf{k} + \mathbf{q}, n' \rangle \times \langle \mathbf{k}, n | \exp[i(\mathbf{q} + \mathbf{G}') \cdot \mathbf{r}] | \mathbf{k} + \mathbf{q}, n' \rangle. \quad (6)$$

With the use of the time-dependent DFT, we can determine the entire interaction density response function through a Dyson-like equation, expanded in plane waves [31,32]:

$$\chi_{GG'}(\mathbf{q}, \omega) = \chi_{GG'}^0(\mathbf{q}, \omega) + \sum_{\mathbf{G}_1, \mathbf{G}_2} \chi_{GG'}^0(\mathbf{q}, \omega) K_{\mathbf{G}_1, \mathbf{G}_2}(\mathbf{q}) \chi_{\mathbf{G}_1, \mathbf{G}_2}(\mathbf{q}, \omega). \quad (7)$$

In this formula, \mathbf{G} and \mathbf{q} are the reciprocal lattice vectors and the corresponding wave vector, and $K_{\mathbf{G}_1, \mathbf{G}_2}$ is the interacting response function. In the random phase approximation, the dielectric function converts to [24]

$$\epsilon_{\mathbf{G}\mathbf{G}'}^{-1}(\mathbf{q}, \omega) = \delta_{\mathbf{G}\mathbf{G}'} - \frac{4\pi}{|\mathbf{q} + \mathbf{G}|^2} \chi_{\mathbf{G}\mathbf{G}'}^0(\mathbf{q}, \omega). \quad (8)$$

The macroscopic dielectric function is defined as [29,30]

$$\epsilon_M(\mathbf{q}, \omega) = \frac{1}{\epsilon_{00}^{-1}(\mathbf{q}, \omega)}. \quad (9)$$

The electron energy loss spectrum (EELS) $L(\mathbf{q}, \omega)$ is calculated by evaluating the imaginary part of the inverse of the macroscopic dielectric function [33,34]:

$$L(\mathbf{q}, \omega) = -\text{Im} \epsilon_M^{-1}(\mathbf{q}, \omega). \quad (10)$$

To accurately describe the interband transitions, we utilize a dense k -point grid of $75 \times 45 \times 1$ and consider up to 80 empty bands. For minor q modes, we use a denser k -point grid of $150 \times 90 \times 1$. Our computations also account for local field effects using an energy of 50 eV and a broadening parameter of $\eta = 0.05$ eV.

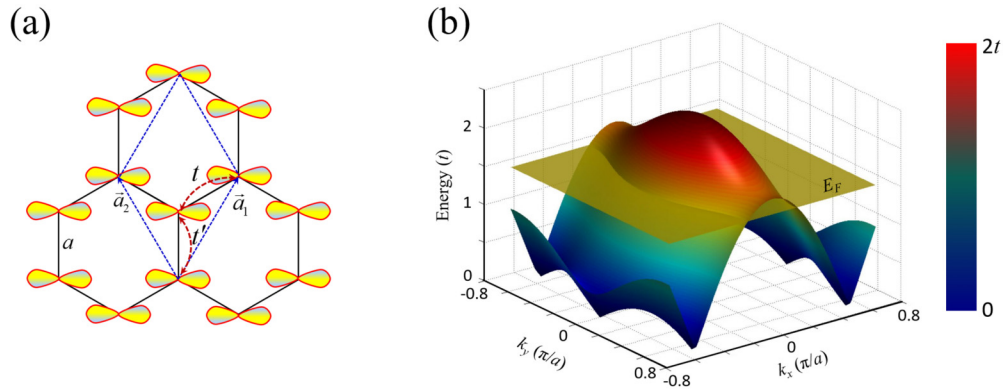


FIG. 1. (a) Schematic representation of anisotropic orbital ordering in a honeycomb lattice. (b) Band profile of the tight-binding (TB) model and the Fermi surface indicated by the intersection lines between the band profile and the plane of $E = E_F$. The Fermi energy (E_F) is set to $1.5t$.

III. RESULTS AND DISCUSSION

A. TB model of anisotropic orbitals

To illustrate the correlation between orbital ordering and the anisotropy of electronic band structures that meet the criteria for a 2D-HM (i.e., metallic in one direction and semi-conducting in another), we begin with a simple TB model of a honeycomb lattice with a p_x atomic orbital at each site, as shown in Fig. 1(a). In view of the in-plane anisotropy of the p_x atomic orbital, we limit our analysis to electron hopping between two adjacent sites with varying hopping parameters,

$-t$ and $-t'$ ($t > 0$; $t' > 0$), as depicted in Fig. 1(a). This approach differs notably from the TB model of graphene, in which the p_z atomic orbitals possess in-plane isotropy. The TB Hamiltonian of the lattice reads

$$H = \begin{bmatrix} 0 & g(\mathbf{k}) \\ g^*(\mathbf{k}) & 0 \end{bmatrix}, \quad (11)$$

with $g(\mathbf{k}) = t\{\exp[i(\frac{\sqrt{3}k_x a}{2} + \frac{k_y a}{2})] + \exp[i(-\frac{\sqrt{3}k_x a}{2} + \frac{k_y a}{2})]\} + t'\exp(-ik_y a)$, which gives the energy spectrum of

$$E_{\pm}(k) = \pm \sqrt{2t^2 + t'^2 + 2t^2 \cos(\sqrt{3}k_x a) + 4tt' \cos\left(\frac{\sqrt{3}}{2}k_x a\right) \cos\left(\frac{3}{2}k_y a\right)}. \quad (12)$$

In this expression, a represents the distance between two adjacent sites. Assuming each site has more than one electron, the E_- band is filled by electrons, while the E_+ band is only partially occupied, resulting in a metallic model. The profile of the E_+ band with $t' = 0.3t$ is plotted in Fig. 1(b). The band exhibits significant anisotropy along the x and y directions, with a dispersive shape along the x direction but a flattened shape along the y direction. By setting the Fermi level (E_F) to $1.5t$, we obtain an open ovelike Fermi surface which is highly anisotropic, as indicated by the intersection between the band profile and the plane of $E = E_F$. The open ovelike Fermi surface implies an anisotropic response of electron motion to the external electric field. Specifically, the electron velocity $v(\mathbf{k}) = \nabla_{\mathbf{k}} E$ perpendicular to the Fermi surface has a significant component along the x direction, indicating high electron conductivity along this direction, according to Eq. (4). On the other hand, the component of $v(\mathbf{k})$ along the y direction $\partial E / \partial k_y$ is negligible, suggesting low conductivity (semiconducting) along this direction. This highly anisotropic conductivity promotes the formation of broadband hyperbolic regime. Furthermore, this principle applies to the distorted honeycomb structure with stretching along the $[110]$ direction.

B. Lattice and electronic structures of XY_2 ($X = \text{Al, Ga, In}$; $Y = \text{S, Se, Te}$) monolayers

In this section, we will demonstrate how to design a 2D material with highly anisotropic electron conductivity, using the TB model. In our analysis, we focus on XY_2 monolayers with rhombic unit cells and a $P2/m$ space group, where $X = \text{Al, Ga, In}$ and $Y = \text{S, Se, Te}$. The Y atoms form a buckled honeycomb sublattice, as depicted in Fig. 2(a). Notably, the Y atoms have a valence of $-\frac{3}{2}$, which is higher than the conventional X_2Y_3 compounds (e.g., Al_2S_3). This results in their p orbitals being partially occupied, making them well suited for the TB model. In the following sections, we will take the AlS_2 monolayer as an example to study the lattice and electronic structures of this anisotropic 2D family. The monolayer consists of an Al plane sandwiched by two S planes with a thickness of 3.0 \AA determined from the distance between the two S planes. Each Al/S atom is coordinated by 6 S/3 Al atoms, with an Al-S bond length of 2.4 \AA . The base vectors have a length of 3.5 \AA , and the angle between them is 49.9° . The phonon spectrum of the AlS_2 monolayer, as shown in Fig. 2(b), is free from imaginary frequency modes, indicating its dynamic stability. We have adopted first-principles molecular dynamics simulations to investigate the thermodynamic

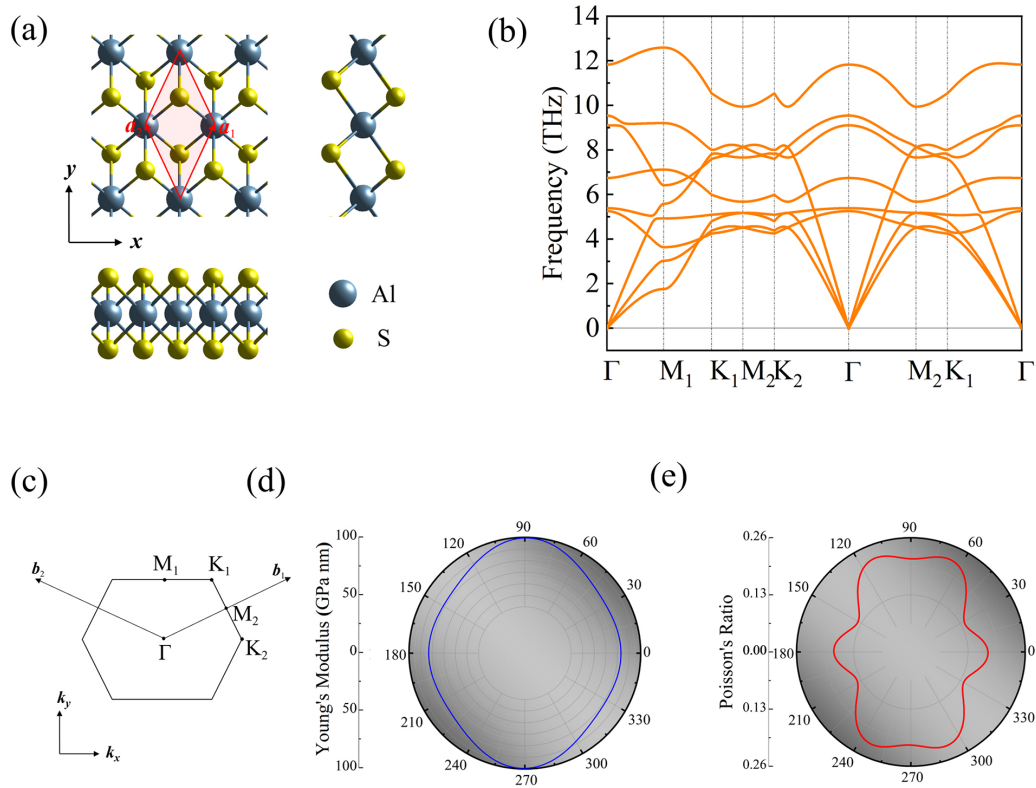


FIG. 2. (a) Top and side views of the crystal structure of AlS₂ monolayer. (b) Phonon spectrum, (c) Brillouin zone, (d) Young's modulus, and (e) Poisson's ratio of AlS₂ monolayer.

stability of the AlS₂ monolayer at a temperature of 800 K [35]. Our results demonstrate that the monolayer is thermodynamically stable under this condition. Furthermore, we have examined the chemical stability of the AlS₂ monolayer by analyzing the decomposition reaction $2\text{AlS}_2 \rightarrow \text{Al}_2\text{S}_3 + \text{S}$. Our calculations indicate that this reaction is endothermic with a reaction enthalpy of ~ 1.12 eV/AlS₂, thus confirming the chemical stability of the monolayer. The lattice parameters and the phonon spectra of other XY₂ monolayers are presented in the Supplemental Material [35]. The angle between the two basis vectors deviates from 60° of a perfect honeycomb lattice. The distorted honeycomb sublattice of Y atoms could enhance the anisotropy of the 2D materials by reducing the magnitude of t' as predicted by the TB model.

Notably, Young's moduli of the AlS₂ monolayer exhibit minimal anisotropy, as demonstrated in Fig. 2(d). The values for the moduli are 82.98 and 99.46 N m⁻¹ along the x and y directions, respectively. While Young's moduli of XY₂ monolayers are larger than those of the MX ($M = \text{Al, Ga, In, Zn, Cd}; X = \text{P, As, Sb, S, Se, Te}; 1.43\text{--}60.72$ N m⁻¹) monolayers [36], they are lower than those of phosphorene (103.32 N m⁻¹) and graphene (354.00 N m⁻¹) [37]. Additionally, the anisotropy of Poisson's ratio of the AlS₂ monolayer is also insignificant, as shown in Fig. 2(e). The weak anisotropy observed in the mechanical properties of the AlS₂ monolayer is correlated with the weak anisotropy in the atomic arrangement of the distorted honeycomb lattice. Additionally, the elastic constants meet the mechanical stability criteria $C_{11}C_{22} - C_{12}^2 > 0$ and $C_{66} > 0$, confirming the mechanical stability of the AlS₂ monolayer. Similar results

for other XY₂ monolayers can be found in the Supplemental Material [35].

Compared with its mechanical properties, the electronic band structures of the AlS₂ monolayer exhibit remarkable anisotropy, as illustrated in Figs. 3(a) and 3(b). It is evident that the AlS₂ monolayer is metallic with two bands across the Fermi level, which predominantly arise from the p_x orbitals of S atoms, in accordance with the TB model. Notably, the metallic features along the Γ -K₂ (x) direction are particularly pronounced. We attribute it to the remarkable overlap of the dispersed S(p_x) orbitals along this direction, as shown in Fig. 3(c), which offers a conducting channel for electron motion. The high Fermi velocity of $\sim 10^6$ m/s suggests the excellent electron conductivity along the x direction. However, along the Γ -M₁ (y) direction, the overlap between the S(p_x) orbitals is less remarkable than that along the Γ -K₂ direction. Consequently, the relevant two bands are flatter and situated above the Fermi level. Therefore, a band gap of 1.74 eV emerges along the Γ -M₁ direction, indicating the semiconducting natures along this direction. This is also consistent with the opened Fermi surfaces shown in Fig. 3(b), which depicts the absence of electronic states along the Γ -M₁ direction. These results agree with the TB model. Similar electronic band structures are also observed in the analogues of the AlS₂ monolayer, as illustrated in Fig. S1 in the Supplemental Material [35].

C. Hyperbolic properties

Utilizing the aforementioned approach, we compute the conductivity tensor. When characterizing the hyperbolic

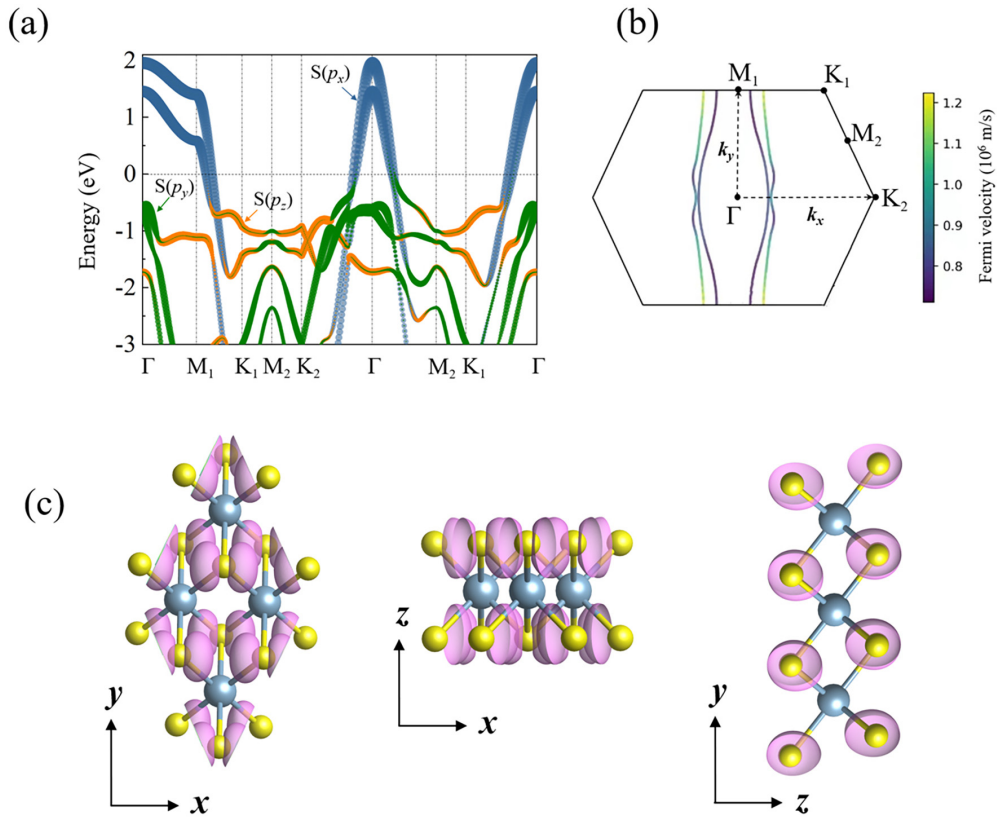


FIG. 3. (a) Orbital-resolved electronic band structure of AlS_2 monolayer. The energy at the Fermi level is set to zero. (b) Fermi surfaces of AlS_2 monolayer. The Fermi velocity is indicated by the color of lines. (c) Top and side views of the electron wave function isosurfaces of the bands across the Fermi level.

properties of a 2D material, the conductivity tensor is a more appropriate descriptor than the permittivity tensor. The real and imaginary components of the conductivity tensor are directly related to the imaginary and real components of the permittivity tensor, respectively. Specifically, the imaginary component of conductivity ($\text{Im}\sigma$) represents the response of the material to an electric field, while the real component ($\text{Re}\sigma$) indicates the extent of energy dissipation due to light absorption.

The hyperbolic regime of a 2D material is characterized by the condition $\text{Im}\sigma_{xx} \times \text{Im}\sigma_{yy} < 0$. Figure 4(a) shows the real and imaginary parts of the conductivity tensor for a AlS_2 monolayer. As seen from this figure, for the frequency range of $0.55 < \omega < 3.8$ eV, the AlS_2 monolayer has $\text{Im}\sigma_{xx} > 0$, $\text{Im}\sigma_{yy} < 0$, indicating that it exhibits hyperbolic behavior. The hyperbolic regime covers a wide range of frequencies, spanning the entire near-infrared, visible, and parts of the ultraviolet bands. This range is much broader than those of other 2D-HMs, such as phosphorene (1.73–1.84 eV) [38], CuB_6 (0.53–1.44 eV), CuB_3 (1.66–3.50 eV) [21], hr - sB (1.0–1.58, 1.84–2.21 eV), and $8Pmmn$ borophene (0.085–0.27, 1.85–2.39 eV) [39]. Moreover, within the hyperbolic regime, both $\text{Re}\sigma_{xx}$ and $\text{Re}\sigma_{yy}$ are very small, except for the peak of $\text{Re}\sigma_{xx}$ near 1.35 eV due to the interband transition, indicating low light absorption loss. The broadband hyperbolic regime and weak light absorption loss of the AlS_2 monolayer make it highly suitable for the propagation of electromagnetic waves in the HMs.

The contributions of the intraband and interband transitions to the conductivity tensor of the AlS_2 monolayer are illustrated in Figs. 4(b) and 4(c). In the case of intraband transitions, $\text{Im}\sigma_{xx}$ exhibits metallic characteristics along the x direction over a wide range of energy, while $\text{Im}\sigma_{yy}$ is nearly zero, indicating semiconducting or insulating features. On the other hand, interband transitions cause a decrease in both $\text{Im}\sigma_{xx}$ and $\text{Im}\sigma_{yy}$, as shown in Fig. 4(c), due to the Kramers-Kronig relation between the real and imaginary parts of the conductivity. The competition between the two types of transitions gives rise to the broadband hyperbolic regime of the AlS_2 monolayer.

To evaluate the hyperbolic performance, we define the quality factor (Q) as

$$Q = -\frac{\text{Im}\sigma_{jj}}{\text{Re}\sigma_{jj}}. \quad (13)$$

Obviously, the quality factor is dependent on the frequency and indicates better performance at higher values. For the AlS_2 monolayer, the Q value is >20 within the hyperbolic region of $2.4 < \omega < 4.6$ eV and reaches a maximal value of 47 at $\hbar\omega = 3.1$ eV. These values are significantly higher than those observed in other materials, such as Al_2O_3 , MgF_2 , and SiO_2 [40].

The excellent hyperbolic properties of the AlS_2 monolayer are attributed to the anisotropic electronic structures. The metallic nature of the material along the x direction gives rise to an inductive response, whereas a capacitive response

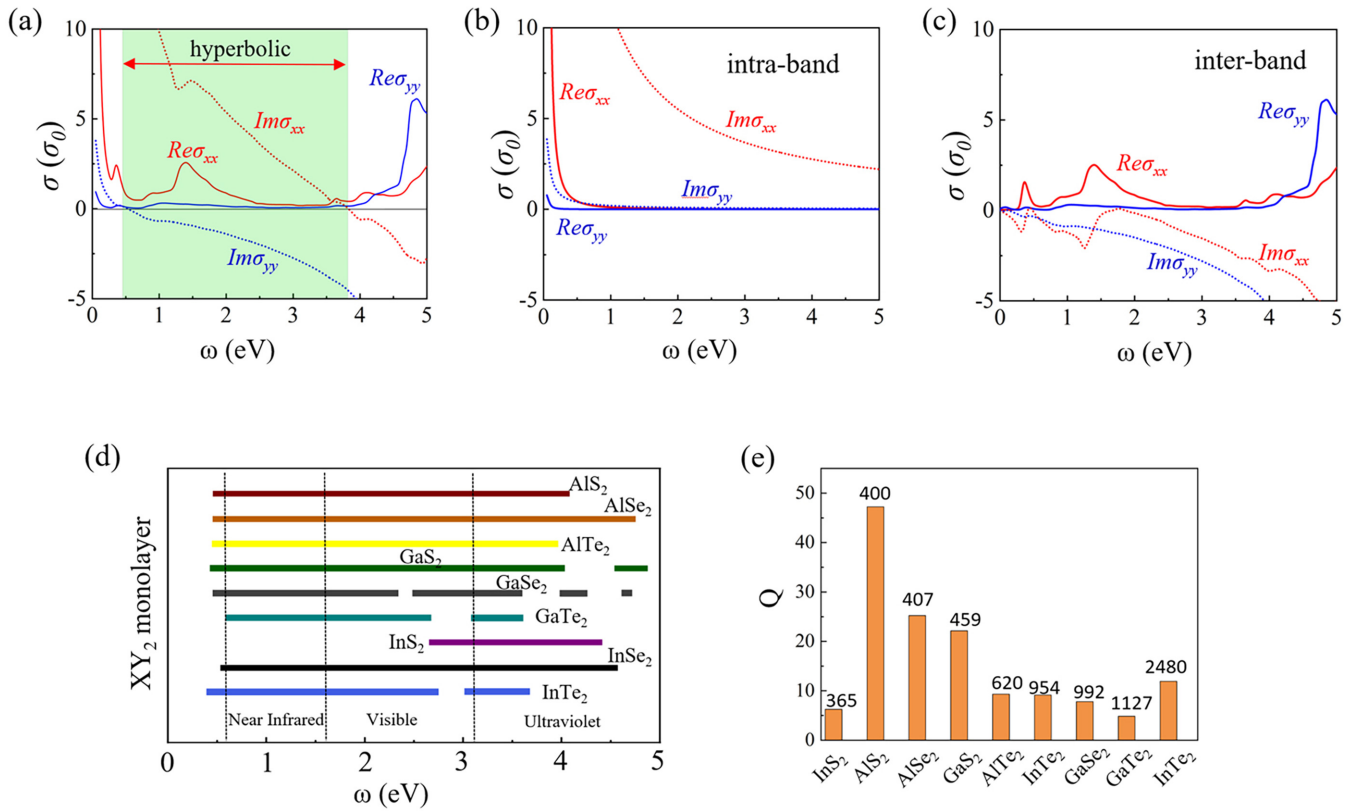


FIG. 4. (a) Conductivity tensor of AlS_2 monolayer. (b) and (c) The intraband and interband contributions to the conductivity tensor. (d) The hyperbolic regimes of XY_2 ($X = Al, Ga, In; Y = S, Se, Te$) monolayers. (e) The maximal quality factor Q of XY_2 monolayers. The numbers show the wavelengths (nm) corresponding to the maximal Q .

is observed along the semiconducting y direction, resulting in a broadband hyperbolic regime. The valence and conduction bands along the Γ - M_1 (y) direction near the Fermi level exhibit distinct orbital features. Specifically, the valence bands arise from the p_y/p_z orbitals of S atoms, while the conduction bands originate from the p_x orbitals of S atoms. However, the transition between these bands is limited due to symmetry constraints, resulting in low light adsorption ability along the y direction in the hyperbolic regime.

The hyperbolic properties described above are commonly observed in the analogues of the AlS_2 monolayer. The hyperbolic regimes of XY_2 ($X = Al, Ga, In; Y = S, Se, Te$) monolayers are plotted in Fig. 4(d). Most of these 2D materials exhibit hyperbolic regimes that span the entire near-infrared to visible range and parts of the ultraviolet range, implying their potential for developing hyperbolic media and device applications. The frequency-dependent conductivity tensors of these materials are presented in the Supplemental Material [35]. The maximal Q and the wavelengths (nm) corresponding to the maximal Q of XY_2 monolayers are plotted in Fig. 4(e). The AlS_2 monolayer has the largest maximal quality factor, followed by $AlSe_2$ and GaS_2 monolayers among these 2D materials.

To examine the effect of the substrate effect on the hyperbolic regime of the AlS_2 monolayer, we place a AlS_2 monolayer on a hBN substrate. The atomic flatness, insulating nature, and chemical inertness of hBN make it an ideal material for supporting 2D materials without significantly

influencing their electronic properties. Our calculations demonstrate that the broadband hyperbolic regime of the isolated AlS_2 monolayer remains intact in the AlS_2 /hBN heterostructure, confirming the robustness of its hyperbolic properties [35]. We attribute it to the wide band gap of hBN and the weak van der Waals interaction between AlS_2 and hBN, which have a minimal impact on the anisotropic electronic properties of the AlS_2 monolayer.

D. Anisotropic plasmonic properties

The anisotropic electronic band structure also leads to the anisotropic plasmonic properties of the AlS_2 monolayer. We begin by examining the plasmons in the AlS_2 monolayer along two specific directions. The dispersion relation of plasmons is depicted by EELS calculated using Eq. (10). Figures 5(a) and 5(b) show EELS of the AlS_2 monolayer along the x and y directions, respectively, where the magnitude of loss function $L(\mathbf{q}, \omega)$ is indicated by color. The anisotropy of the plasmon modes along the x and y directions is quite evident. Along the x direction, the frequency of the plasmons increases rapidly with the wave vector and can attain 4.73 eV before entering the single-particle excitation region and decaying into electron-hole pairs. This value is significantly higher than those reported in other 2D materials, such as $TaSe_2$ (1.0 eV) [41], β_{12} borophene (1.8 eV) [42], and LiC_2 (2.7 eV) [43]. On the other hand, the energy of the plasmons along the y direction increases slowly, and the plasmons quickly decay

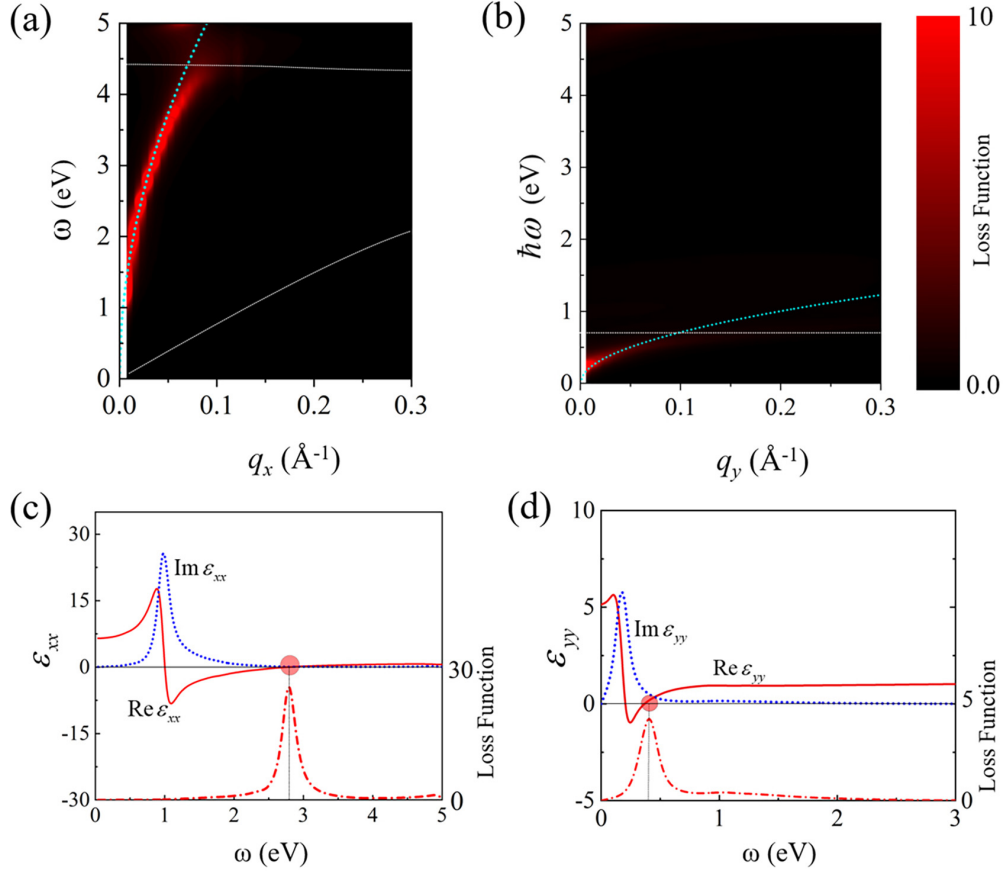


FIG. 5. The electron energy loss spectra (EELS) of AlS₂ monolayer along the (a) $\Gamma-K_2$ (x) direction and (b) $\Gamma-M_1$ (y) direction. The cyan dotted lines represent the fitting data using the expression $\omega = \alpha\sqrt{q}$, with $\alpha = 16.7$ and 2.24 eV \AA , respectively. The white dotted lines indicate the boundaries of the single-particle excitation (SPE) regions. The dielectric function (top panel) and the loss function (bottom panel) of AlS₂ monolayer at (c) $q_x = 0.028 \text{ \AA}^{-1}$ and (d) $q_y = 0.011 \text{ \AA}^{-1}$. The red circles denote the zeros of $\text{Re}\epsilon$.

into electron-hole pairs. The undamped plasmons along the x direction are more prominent from the dielectric function and electron loss function shown in Fig. 5(c). At the sampling frequency, both real and imaginary parts of the dielectric function are zero accompanied by a sharp peak of the loss function, which is the hallmark of undamped plasmons. Undamped plasmons in such a wide energy region are rarely observed in 2D materials.

According to the 2D electron gas model, the plasmon in 2D materials has the dispersion relation:

$$\omega = \alpha\sqrt{q}, \quad (14)$$

with $\alpha = (\frac{ne^2}{2m^*\epsilon_0})^{1/2}$. In this expression, n and m^* are the density and effective mass of carriers, ϵ_0 is the permittivity of the vacuum. The plasmon dispersion of the AlS₂ monolayer along the x and y directions can be well fitted by Eq. (14), as shown in Fig. 5. Assuming each S atom contributes one electron, the carrier density of the AlS₂ monolayer is $2.2 \times 10^{15} \text{ cm}^{-2}$. The effective masses of the carrier are then fitted to $0.55 m_e$ and $30.25 m_e$ along the x and y directions, respectively, where m_e represents the mass of a free electron. Interestingly, the anisotropy of electron motion characterized by the ratio of carrier masses between the y and x directions $m_y^*/m_x^* \approx 56$ is significantly larger than those of other

2D-HMs, such as boron polymorphs (2.71, 3.71) [44], monolayer black phosphorus (4.21) [45], and MoOCl₂ (23.56) [20]. Unsurprisingly, anisotropic plasmons are a common feature of the analogues of the AlS₂ monolayer with similar anisotropic electronic structures, as demonstrated in the Supplemental Material [35].

E. Directional surface plasmons

Finally, we investigate the potential directional propagation of surface plasmons on an AlS₂ monolayer in the hyperbolic regime. Surface plasmons are excited by a z -polarized electric dipole positioned above the sheet, as depicted in Fig. 6(a). By numerically solving Maxwell's equations using a commercial finite-difference time-domain method, we can determine the dispersion relation and distribution of the surface plasmon electric field \mathbf{E} [35]. These calculations utilize the conductivities derived from our first-principles calculations. We examine the behavior of the AlS₂ monolayer at four frequencies: $\omega = 0.30, 0.65, 1.75,$ and 3.35 eV . The corresponding conductivities, σ_{xx} and σ_{yy} , are determined to be $0.084 \text{ mS} + 2.13i \text{ mS}$, $0.029 \text{ mS} + 0.976i \text{ mS}$, $0.084 \text{ mS} + 0.386i \text{ mS}$, $0.012 \text{ mS} + 0.07i \text{ mS}$, and $0.0036 \text{ mS} + 0.0234i \text{ mS}$, $0.029 \text{ mS} - 0.0138i \text{ mS}$, $0.0132 \text{ mS} - 0.0696i \text{ mS}$, $0.0048 \text{ mS} - 0.2i \text{ mS}$ for σ_{xx} and

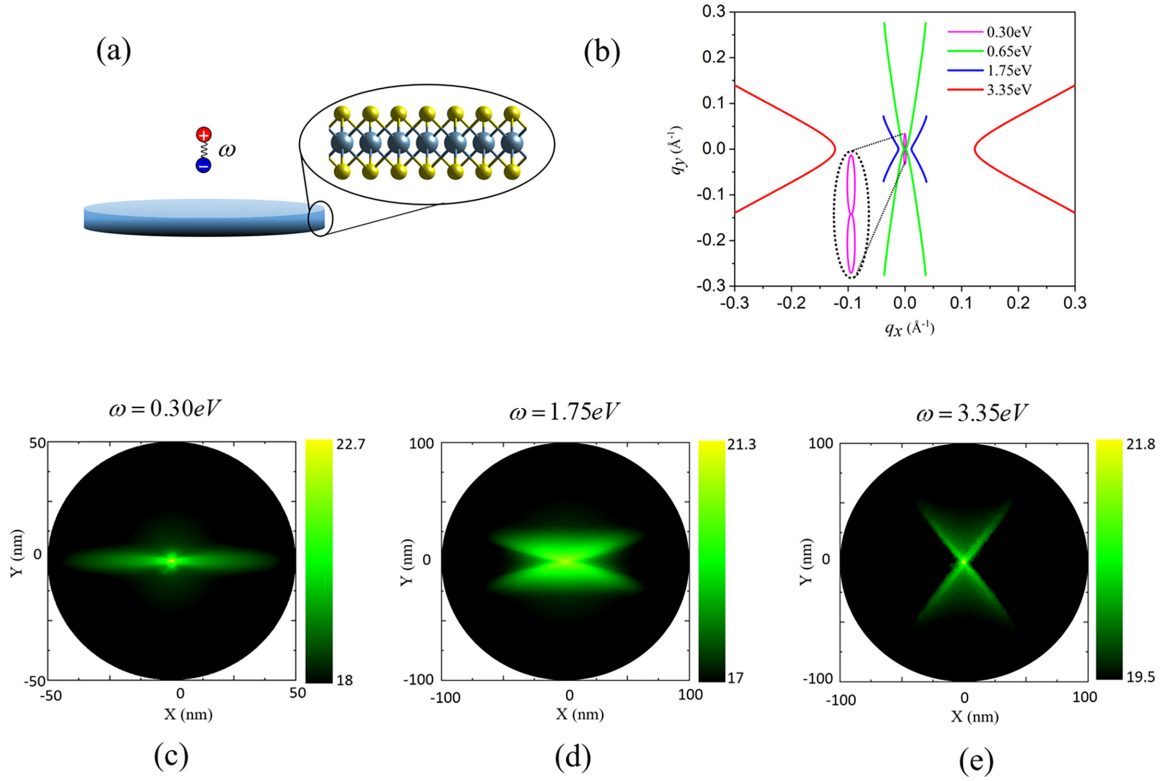


FIG. 6. (a) Schematic representation of surface plasmons on an AlS₂ monolayer disk excited by a vertically polarized electric dipole. (b) The isofrequency profiles of the surface plasmons on an AlS₂ monolayer disk with $\omega = 0.30, 0.65, 1.75,$ and 3.35 eV. (c)–(e) The spatial distribution of electric field E of the surface plasmons at different frequencies.

σ_{yy} , respectively, $i = \sqrt{-1}$. The isofrequency profiles for the frequencies of 0.65, 1.75, and 3.35 eV, which fall within the hyperbolic regime, exhibit hyperbolic characteristics in momentum space, as shown in Fig. 6(b). However, at the frequency of $\omega = 0.30$ eV, beyond the hyperbolic regime, we observe an ellipselike isofrequency curve. The spatial distribution of the electric field on the sheet confirms the directional propagation features of the surface plasmons in natural 2D-HMs, as the energy of the surface plasmons is channeled as narrow beams, as illustrated in Figs. 6(c)–6(e). Interestingly, we also observe remarkable directional propagation of surface plasmons at the frequency of 0.30 eV beyond the hyperbolic regime, as shown in Fig. 6(c). This behavior is attributed to the unique ultrahigh anisotropy of the conductivities along the x and y directions, where the conductivity along the x direction is almost two orders of magnitude larger than that along the y direction.

In view of the ultralow energy loss of an AlS₂ monolayer represented by $\text{Im}\sigma \gg \text{Re}\sigma$, the dispersion relation of the surface plasmons can be determined by the expression [46]:

$$\frac{q_x^2}{\text{Im}\sigma_{yy}} + \frac{q_y^2}{\text{Im}\sigma_{xx}} \approx 2p\omega \left(\frac{\varepsilon_0}{\text{Im}\sigma_{xx} \times \text{Im}\sigma_{yy}} - \frac{\mu_0}{4} \right), \quad (15)$$

where $k_0 = \omega\sqrt{\varepsilon_0\mu_0}$, ε_0 , and μ_0 are, respectively, the vacuum wave number, permittivity, and permeability, and $p = \sqrt{q_x^2 + q_y^2 - k_0^2}$. This gives a hyperbolic dispersion for

$\text{Im}\sigma_{xx} \times \text{Im}\sigma_{yy} < 0$ (corresponding to the hyperbolic regime of a 2D material) with the asymptotes of

$$q_y = \pm q_x \left| \frac{\text{Im}\sigma_{xx}}{\text{Im}\sigma_{yy}} \right|^{1/2}. \quad (16)$$

The isofrequency profiles obtained from our calculations align with Eq. (15), as illustrated in Fig. 6(b), further supporting the accuracy and validity of our calculations. The direction of the surface plasmon beams given by the group velocity $v_g = \nabla_{\mathbf{q}}\omega(\mathbf{q})$ that represents the energy propagation normal to the hyperbolic asymptotes is

$$y = \pm x \left| \frac{\text{Im}\sigma_{yy}}{\text{Im}\sigma_{xx}} \right|^{1/2}. \quad (17)$$

The propagation angle determined by the surface plasmon electric field distribution agrees with Eq. (17). Additionally, low energy loss is crucial for achieving directional surface plasmon propagation. These findings imply that the AlS₂ monolayer has the potential to guide anisotropic plasmons, highlighting their promising applications in nanophotonics and plasmonic devices.

IV. CONCLUSIONS

In summary, we propose a design principle for 2D-HMs based on the in-plane anisotropic p_x orbitals. Through first-principles calculations, we identify a promising family of 2D-HMs, including the AlS₂ monolayer and its

analogues XY_2 ($X = \text{Al, Ga, In}$; $Y = \text{S, Se, Te}$). In this paper, we reveal that the inherently anisotropic p_x orbitals contribute to the anisotropic electronic bands near the Fermi level, resulting in an open olivelike Fermi surface in these 2D materials. This unique electronic structure imparts metallic properties along the x direction but semiconducting properties along the y direction, rendering broadband hyperbolic regimes that span the visible light range to the ultraviolet spectrum. Furthermore, we observe the emergence of undamped plasmons along the x direction with a maximum wave vector of $\sim 0.16 \text{ \AA}^{-1}$ and frequency of 4.6 eV. Conversely, plasmons propagating along the y direction exhibit lower frequencies ($< 0.6 \text{ eV}$) and decay rapidly to electron-hole pairs in the AlS_2 monolayer. The

strong anisotropic conductivity and low energy loss of these materials also support the propagation of highly directional hyperbolic surface plasmons. Overall, in this paper, we uncover the correlation between the electronic structure and plasmonic properties of these 2D-HMs, which could pave the way for the design and utilization of natural 2D-HMs in various technological applications.

ACKNOWLEDGMENT

This paper is supported by the National Natural Science Foundation of China (Grant No. 12074218) and the Taishan Scholar Program of Shandong Province.

-
- [1] J. Yao, X. D. Yang, X. B. Yin, G. Bartal, and X. Zhang, Three-dimensional nanometer-scale optical cavities of indefinite medium, *Proc. Natl. Acad. Sci. USA* **108**, 11327 (2011).
- [2] X. D. Yang, J. Yao, J. Rho, X. B. Yin, and X. Zhang, Experimental realization of three-dimensional indefinite cavities at the nanoscale with anomalous scaling laws, *Nat. Photonics* **6**, 450 (2012).
- [3] D. Lu, J. J. Kan, E. E. Fullerton, and Z. W. Liu, Enhancing spontaneous emission rates of molecules using nanopatterned multilayer hyperbolic metamaterials, *Nat. Nanotechnol.* **9**, 48 (2014).
- [4] Z. W. Liu, H. Lee, Y. Xiong, C. Sun, and X. Zhang, Far-field optical hyperlens magnifying sub-diffraction-limited objects, *Science* **315**, 1686 (2007).
- [5] S. V. Boriskina, H. Ghasemi, and G. Chen, Plasmonic materials for energy: From physics to applications, *Mater. Today* **16**, 375 (2013).
- [6] J. Yao, Z. W. Liu, Y. M. Liu, Y. Wang, C. Sun, G. Bartal, A. M. Stacy, and X. Zhang, Optical negative refraction in bulk metamaterials of nanowires, *Science* **321**, 930 (2008).
- [7] A. J. Hoffman, L. Alekseyev, S. S. Howard, K. J. Franz, D. Wasserman, V. A. Podolskiy, E. E. Narimanov, D. L. Sivco, and C. Gmachl, Negative refraction in semiconductor metamaterials, *Nat. Mater.* **6**, 946 (2007).
- [8] J. B. Sun, J. Zhou, B. Li, and F. Y. Kang, Indefinite permittivity and negative refraction in natural material: Graphite, *Appl. Phys. Lett.* **98**, 101901 (2011).
- [9] F. N. Xia, H. Wang, D. Xiao, M. Dubey, and A. Ramasubramaniam, Two-dimensional material nanophotonics, *Nat. Photonics* **8**, 899 (2014).
- [10] H. Gao, Z. H. Wang, X. K. Ma, X. M. Zhang, W. F. Li, and M. W. Zhao, Hyperbolic dispersion and negative refraction in a metal-organic framework Cu-BHT, *Phys. Rev. Mater.* **3**, 065206 (2019).
- [11] M. N. Gjerding, R. Petersen, T. G. Pedersen, N. A. Mortensen, and K. S. Thygesen, Layered van der Waals crystals with hyperbolic light dispersion, *Nat. Commun.* **8**, 320 (2017).
- [12] H. Gao, X. M. Zhang, W. F. Li, and M. W. Zhao, Tunable broadband hyperbolic light dispersion in metal diborides, *Opt. Express* **27**, 36911 (2019).
- [13] J. B. Sun, N. M. Litchinitser, and J. Zhou, Indefinite by nature: From ultraviolet to terahertz, *ACS Photonics* **1**, 293 (2014).
- [14] J. D. Caldwell, A. V. Kretinin, Y. G. Chen, V. Giannini, M. M. Fogler, Y. Francescato, C. T. Ellis, J. G. Tischler, C. R. Woods, and A. J. Giles, Sub-diffractive volume-confined polaritons in the natural hyperbolic material hexagonal boron nitride, *Nat. Commun.* **5**, 5221 (2014).
- [15] J. S. Gomez-Diaz and A. Alù, Flatland optics with hyperbolic metasurfaces, *ACS Photonics* **3**, 2211 (2016).
- [16] W. L. Ma, P. Alonso-González, S. J. Li, A. Y. Nikitin, J. Yuan, J. Martín-Sánchez, J. Taboada-Gutiérrez, I. Amenabar, P. N. Li, and S. Vélez, In-plane anisotropic and ultra-low-loss polaritons in a natural van der Waals crystal, *Nature (London)* **562**, 557 (2018).
- [17] H. W. Wang and T. Low, Hyperbolicity in two-dimensional transition metal ditellurides induced by electronic bands nesting, *Phys. Rev. B* **102**, 241104(R) (2020).
- [18] S. Edalati-Boostan, C. Cocchi, and C. Draxl, MoTe_2 as a natural hyperbolic material across the visible and the ultraviolet region, *Phys. Rev. Mater.* **4**, 085202 (2020).
- [19] E. van Veen, A. Nemilentsau, A. Kumar, R. Roldán, M. I. Katsnelson, T. Low, and S. J. Yuan, Tuning Two-Dimensional Hyperbolic Plasmons in Black Phosphorus, *Phys. Rev. Appl.* **12**, 014011 (2019).
- [20] H. Gao, C. Ding, L. Sun, X. K. Ma, and M. W. Zhao, Robust broadband directional plasmons in a MoOCl_2 monolayer, *Phys. Rev. B* **104**, 205424 (2021).
- [21] W. H. Geng, H. Gao, C. Ding, L. Sun, X. K. Ma, Y. Y. Li, and M. W. Zhao, Highly-anisotropic plasmons in two-dimensional hyperbolic copper borides, *Opt. Express* **30**, 5596 (2022).
- [22] G. Kresse and J. Furthmüller, Efficient iterative schemes for *ab initio* total-energy calculations using a plane-wave basis set, *Phys. Rev. B* **54**, 11169 (1996).
- [23] J. Enkovaara, C. Rostgaard, J. J. Mortensen, J. Chen, M. Dulak, L. Ferrighi, J. Gavnholt, C. Glinsvad, V. Haikola, H. A. Hansen *et al.*, Electronic structure calculations with GPAW: A real-space implementation of the projector augmented-wave method, *J. Phys. Condens. Matter* **22**, 253202 (2010).
- [24] J. Yan, J. J. Mortensen, K. W. Jacobsen, and K. S. Thygesen, Linear density response function in the projector augmented wave method: Applications to solids, surfaces, and interfaces, *Phys. Rev. B* **83**, 245122 (2011).
- [25] P. E. Blöchl, Projector augmented-wave method, *Phys. Rev. B* **50**, 17953 (1994).

- [26] J. P. Perdew, K. Burke, and M. Ernzerhof, Generalized Gradient Approximation Made Simple, *Phys. Rev. Lett.* **77**, 3865 (1996).
- [27] L. A. Falkovsky and A. A. Varlamov, Space-time dispersion of graphene conductivity, *Eur. Phys. J. B* **56**, 281 (2007).
- [28] V. P. Gusynin, S. G. Sharapov, and J. P. Carbotte, Unusual Microwave Response of Dirac Quasiparticles in Graphene, *Phys. Rev. Lett.* **96**, 256802 (2006).
- [29] N. Wiser, Dielectric constant with local field effects included, *Phys. Rev.* **129**, 62 (1963).
- [30] S. L. Adler, Quantum theory of the dielectric constant in real solids, *Phys. Rev.* **126**, 413 (1962).
- [31] E. Runge and E. K. U. Gross, Density-Functional Theory for Time-Dependent Systems, *Phys. Rev. Lett.* **52**, 997 (1984).
- [32] M. Petersilka, U. J. Gossmann, and E. K. U. Gross, Excitation Energies from Time-Dependent Density-Functional Theory, *Phys. Rev. Lett.* **76**, 1212 (1996).
- [33] P. Nozieres and D. Pines, Electron interaction in solids—Characteristic energy loss spectrum, *Phys. Rev.* **113**, 1254 (1959).
- [34] H. Gao, C. Ding, J. Son, Y. Y. Zhu, M. Z. Wang, Z. G. Yu, J. N. Chen, L. Wang, S. A. Chambers, T. W. Noh *et al.*, Ultraflat and long-lived plasmons in a strongly correlated oxide, *Nat. Commun.* **13**, 4662 (2022).
- [35] See Supplemental Material at <http://link.aps.org/supplemental/10.1103/PhysRevB.107.195410> for the structural and mechanical parameters, phonon spectra, and molecular dynamics simulations of XY_2 ($X = \text{Al, Ga, In}$; $Y = \text{S, Se, Te}$) monolayers; the electronic band structures of XY_2 ($X = \text{Al, Ga, In}$; $Y = \text{S, Se, Te}$) monolayers; the frequency-dependent conductivity tensors of XY_2 ($X = \text{Al, Ga, In}$; $Y = \text{S, Se, Te}$) monolayers; the frequency-dependent conductivity tensors of an AlS_2 monolayer on hBN; the EELS spectra of XY_2 ($X = \text{Al, Ga, In}$; $Y = \text{S, Se, Te}$) monolayers; and the computational details for directional surface plasmons.
- [36] X. K. Ma, J. Liu, Y. C. Fan, W. F. Li, J. F. Hu, and M. W. Zhao, Giant negative Poisson's ratio in two-dimensional V-shaped materials, *Nano. Adv.* **3**, 4554 (2021).
- [37] E. Cadelano, P. L. Palla, S. Giordano, and L. Colombo, Elastic properties of hydrogenated graphene, *Phys. Rev. B* **82**, 235414 (2010).
- [38] F. J. Wang, C. Wang, A. Chaves, C. Y. Song, G. W. Zhang, S. Y. Huang, Y. C. Lei, Q. X. Xing, L. Mu, Y. G. Xie *et al.*, Prediction of hyperbolic exciton-polaritons in monolayer black phosphorus, *Nat. Commun.* **12**, 5628 (2021).
- [39] Z. Torbatian, D. Novko, and R. Asgari, Hyperbolic plasmon modes in tilted Dirac cone phases of borophene, *Phys. Rev. B* **104**, 075432 (2021).
- [40] K. Korzeb, M. Gajc, and D. A. Pawlak, Compendium of natural hyperbolic materials, *Opt. Express* **23**, 25406 (2015).
- [41] K. Andersen and K. S. Thygesen, Plasmons in metallic monolayer and bilayer transition metal dichalcogenides, *Phys. Rev. B* **88**, 155128 (2013).
- [42] C. Lian, S. Q. Hu, J. Zhang, C. Cheng, Z. Yuan, S. W. Gao, and S. Meng, Integrated Plasmonics: Broadband Dirac Plasmons in Borophene, *Phys. Rev. Lett.* **125**, 116802 (2020).
- [43] L. Marusic and V. Despoja, Prediction of measurable two-dimensional plasmons in Li-intercalated graphene LiC_2 , *Phys. Rev. B* **95**, 201408(R) (2017).
- [44] Y. F. Huang, S. N. Shirodkar, and B. I. Yakobson, Two-dimensional boron polymorphs for visible range plasmonics: A first-principles exploration, *J. Am. Chem. Soc.* **139**, 17181 (2017).
- [45] F. P. Jin, R. Roldán, M. I. Katsnelson, and S. J. Yuan, Screening and plasmons in pure and disordered single- and bilayer black phosphorus, *Phys. Rev. B* **92**, 115440 (2015).
- [46] A. Nemilentsau, T. Low, and G. Hanson, Anisotropic 2D Materials for Tunable Hyperbolic Plasmonics, *Phys. Rev. Lett.* **116**, 066804 (2016).